

MAGNETOHYDRODYNAMIC SIMULATIONS OF THE SOLAR CORONA AND SOLAR WIND USING A BOUNDARY TREATMENT TO LIMIT SOLAR WIND MASS FLUX

KEIJI HAYASHI

W. W. Hansen Experimental Physics Laboratory, Stanford University, Stanford, CA 94305; keiji@quake.stanford.edu

Received 2005 May 10; accepted 2005 August 2

ABSTRACT

Magnetohydrodynamic simulations of the solar corona and solar wind are sensitive to conditions in the sub-Alfvénic plasma at the base of the solar corona because the structure of the simulated solar corona is determined by the pressure balance of the plasma and the magnetic field. Therefore, it is important to construct an adequate boundary treatment for the sub-Alfvénic surface, and it is highly preferable to build the model from observation-based constraints and basic mathematical theories. We examine new boundary treatments based on the “projected normal characteristic method” for the MHD simulation of the trans-Alfvénic solar wind and solar corona. Our new boundary treatment limits the mass flux escaping through the solar surface. This limit is set to match the solar wind mass flux *Ulysses* measured during its first fast-latitude scan of the heliosphere. In addition, combining the projected normal characteristic method and the mass flux limit, the model produces reasonable contrasts of the plasma temperature and density between the coronal hole and streamer. A two-dimensional version of the time-dependent MHD simulation with the new boundary treatment is tested using the axisymmetric dipole and quadrupole components of the solar magnetic field observed at solar minimum. The new boundary treatment can be characterized by the specific heat ratio on the surface, and we examined several cases. The solar wind computed with the new boundary treatment matches the *Ulysses* measurement at $r > 1$ AU quite well and simultaneously has good contrasts with coronal plasma parameters near the Sun.

Subject headings: methods: numerical — MHD — solar wind — Sun: corona

1. INTRODUCTION

Time-dependent multidimensional MHD simulation provides a powerful approach to study the dynamics of the solar wind and solar corona. Because the solar wind is trans-Alfvénic, only the time relaxation by time-dependent MHD simulation method is capable of constructing a general multidimensional structure of the solar wind from the sub-Alfvénic solar surface to the super-Alfvénic interplanetary space (e.g., Steinolfson et al. 1982; Han et al. 1988; Linker et al. 1990; Washimi & Sakurai 1993; Wang et al. 1993; Usmanov 1993).

Observational data of the solar photospheric magnetic field have been used to define realistic situations and determine the multidimensional solution of the solar wind during interesting periods (e.g., Usmanov & Dryer 1995; Riley et al. 1997; Linker et al. 1999; Mikić et al. 1999; Usmanov & Goldstein 2003). The numerically steady solar wind that results can also be used as the background in simulations tracing the response to eruptive events such as flares and coronal mass ejections (e.g., Wu et al. 1983, 2001; Smith & Dryer 1990; Dryer et al. 1991; Detman et al. 1991; Groth et al. 2000).

Values for the plasma density and temperature on the solar surface must also be determined to begin an MHD simulation of the trans-Alfvénic solar wind. However, because of difficulties in observation, no well-established scheme exists to determine the boundary distribution of the solar surface plasma density, temperature, and velocity at the coronal base ($\sim 1.01 R_{\odot}$) from which the simulation region generally starts. Therefore, many simulation studies simply assign a uniform temperature of $(1-2) \times 10^6$ K and a plasma number density of $(1-2) \times 10^8$ cm $^{-3}$. These given values can be validated after the simulation completes. However, it is highly preferable to constrain these values from the available measurements and theories in physics and mathematics.

Ulysses measured the solar wind over a wide range of heliographic latitudes, and this can give useful constraints to the simulation. The data obtained during its first fast latitude scan in 1994–1995 are especially helpful for simulation studies because this period is at the solar minimum activity phase and the solar magnetic field had a simple dipole-like structure. We here consider two properties of the solar wind measured by *Ulysses* in 1994–1995. One is the solar wind proton flux escaping from the Sun. The average flux was about 2×10^8 cm $^{-2}$ s $^{-1}$ normalized to 1 AU (e.g., Neugebauer 1999). This proton flux is equivalent to 1×10^{13} cm $^{-2}$ s $^{-1}$, or 1×10^8 km s $^{-1}$ cm $^{-3}$ at $1 R_{\odot}$. Considering that the open-field regions at solar minimum activity phase cover about 10%–15% of the entire solar surface, we can estimate the typical average proton flux escaping through the solar surface,

$$\langle NV_r \rangle = (6-10) \times 10^8 \text{ km s}^{-1} \text{ cm}^{-3}. \quad (1)$$

Another property is inferred from the analysis by Geiss et al. (1995), who showed that the temperature at the origin of the fast solar wind tends to be lower (~ 1.1 MK) than that of the slower solar wind (~ 1.7 MK).

In addition to the temperature contrast at the coronal base obtained from *Ulysses* measurements, we can also determine the typical contrast of coronal density from analysis of measurements of the solar corona, such as the SPARTAN campaign (e.g., Fisher & Guhathakurta 1994), *Yohkoh* Soft X-Ray Telescope data (e.g., Aschwanden & Acton 2001), the *Solar and Heliospheric Observatory* (*SOHO*) EUV Imaging Telescope (EIT; e.g., Gallagher et al. 1999), and the *SOHO* Large Angle and Spectrometric Coronagraph Experiment (LASCO-C2; e.g., Frazin & Janzen 2002). The density contrast between the coronal hole and streamer regions varies with observing instrument, time, and height, but

it typically ranges from 3 to 5 near the solar surface and from 5 to 10 at several solar radii. Such a high density contrast is also a good target feature to reproduce with the simulation.

In the practice of MHD simulations, the boundary treatment on the solar surface is important. Because the plasma flow near the solar surface is sub-Alfvénic, there is nonlinear MHD interaction between the solar surface and corona. Therefore, MHD simulations with a simple boundary condition, such as the fixed boundary, may be unable to produce steady coronal structure, as pointed out by Wu et al. (1996).

The projected normal characteristic method has been developed to deal with the temporal variation of MHD variables on the sub-Alfvénic simulation boundary surface (Nakagawa & Steinolfson 1976; Nakagawa 1980, 1981a, 1981b; Nakagawa et al. 1987; Wu & Wang 1987). It uses the concept of characteristics in a hyperbolic system (e.g., Jeffrey & Taniuti 1964). The advantage of time-dependent MHD simulation using this method is that the computed temporal evolution of MHD variables on the sub-Alfvénic computational boundary will match both the governing MHD equation and the given boundary conditions. There have been several successful simulation studies in various areas of solar physics using this method (e.g., Wu et al. 2001).

In this paper, we consider a new boundary treatment model for MHD simulation of the solar corona and solar wind. Our boundary treatment has three notable features. (1) It is based on the concept of the projected normal characteristic method. (2) The solar surface mass flux is limited so that the simulated solar wind mass flux will match the *Ulysses* measurements. (3) It produces a higher, more realistic contrast of the plasma conditions between the coronal hole and streamer. The simulated results satisfy the MHD equations fully, from the inner boundary to the outer boundary, and, at the same time, have good agreements with the observed solar wind and corona at two different heliocentric distances. In addition, the limit of the mass flux will generate adequate contrast of the plasma density and temperature; therefore, our boundary treatment will be a powerful approach to retrieve the three-dimensional structure of the solar corona and solar wind.

We provide a general description of the MHD code in § 2. Our boundary model is described in § 3, and its details are in Appendix B. To test our new boundary treatment, we carried out two-dimensional MHD simulations for $1.01 R_{\odot} < r < 300 R_{\odot}$. In order to compare the simulation results with the *Ulysses* data, we use the observed axisymmetric dipole and quadrupole components of the solar magnetic field of 1995 April as one of the boundary conditions. The simulation results are shown in § 4, and the discussion is presented in § 5.

2. METHOD

2.1. Basic Equations

The basic equations governing the simulated solar wind are the time-dependent MHD equations in the frame rotating with solar sidereal angular velocity Ω ,

$$\frac{\partial \varrho}{\partial t} = -\nabla \cdot (\varrho \mathbf{V}), \quad (2)$$

$$\begin{aligned} \frac{\partial(\varrho \mathbf{V})}{\partial t} = & -\nabla \cdot \left(P_g + \varrho \mathbf{V} \mathbf{V} - \frac{1}{4\pi} \mathbf{B} \mathbf{B} + \frac{B^2}{8\pi} \right) \\ & + \varrho [\mathbf{g} + (\Omega \times \mathbf{r}) \times \Omega + 2\mathbf{V} \times \Omega], \end{aligned} \quad (3)$$

$$\frac{\partial \mathbf{B}}{\partial t} = -\nabla (\mathbf{V} \mathbf{B} - \mathbf{B} \mathbf{V}), \quad (4)$$

and

$$\begin{aligned} \frac{\partial \mathcal{E}}{\partial t} = & -\nabla \cdot \left[\left(\mathcal{E} + P_g + \frac{B^2}{8\pi} \right) \mathbf{V} - \frac{1}{4\pi} \mathbf{B} (\mathbf{V} \cdot \mathbf{B}) \right] \\ & + \varrho \mathbf{V} \cdot [\mathbf{g} + (\Omega \times \mathbf{r}) \times \Omega], \end{aligned} \quad (5)$$

where ϱ , \mathbf{V} , \mathbf{B} , P_g , \mathcal{E} , \mathbf{r} , t , \mathbf{g} , and γ are the mass density, velocity of the plasma flow viewed in the rotating frame, magnetic field vector, gas pressure, energy density $\mathcal{E} = \varrho v^2/2 + P_g/(\gamma - 1) + B^2/2$, position vector originating at the center of the Sun, time, solar gravitational force $\mathbf{g} = -GM/r^3 \cdot \mathbf{r}$, and specific heat ratio, respectively. This study neglects the solar differential rotation for simplicity, and the sidereal angular velocity of the solar rotation, $|\Omega|$, is taken to be $2\pi/25.3$ radian day $^{-1}$ (or 14.2 day $^{-1}$). The specific heat ratio γ is assumed to be 1.05 and constant everywhere so that the trans-Alfvénic solar wind will be obtained.

2.2. Simulation Code

The grid system was constructed in the spherical coordinate system covering the heliocentric distance from 1 to 300 R_{\odot} . The cell sizes along the radius Δr are fixed at 0.01 R_{\odot} near the solar surface in order to treat the steep gradient of density. Beyond 1.1 R_{\odot} , Δr is set proportional to $\ln r$ in the trans-Alfvénic region and proportional to \sqrt{r} in more distant regions, so that a total of 256 grid points can cover from 1.01 to 300 R_{\odot} . The grid size at the outermost several grid points is fixed at 3.5 R_{\odot} . The latitude from the north pole ($\theta = 0$) to the south pole ($\theta = \pi$) is also covered by the grid points with the constant angular interval $\Delta\theta$ equal to $\pi/128$.

The MHD simulation code of our model is based on the concept of total variation diminishing (TVD; e.g., Harten 1983; Brio & Wu 1988) and the monotonic upstream scheme for conservation laws (MUSCL; van Leer 1979). The finite-volume method (e.g., Tanaka 1995) is also used. Letting the column vector \mathbf{U} represent the dependent variables in order,

$$\mathbf{U} = (\varrho, \varrho V_r, \varrho V_{\theta}, \varrho V_{\phi}, B_r, B_{\theta}, B_{\phi}, \mathcal{E})^T, \quad (6)$$

the discretized form of the right-hand side of the governing equations (2)–(5) can be written as

$$\text{RHS}_m = -\frac{1}{\Delta V} \sum \mathbf{F}_m \cdot \mathbf{n} \Delta s + S_m, \quad (7)$$

where the subscript m denotes variables of \mathbf{U} in the order of equation (6), and \mathbf{F} , \mathbf{n} , and Δs represent the flux vector, the vector normal to the cell boundary surface, and the area of the cell boundary, respectively. The volume of the numerical cell, ΔV , is equal to $(\Delta r^3/3)[\Delta(-\cos\theta)(\Delta\phi)]$. The area of the cell interface, Δs , is set to $r^2\Delta(-\cos\theta)\Delta\phi$, $\Delta(r^2/2)(\sin\theta)\Delta\phi$, and $\Delta(r^2/2)\Delta\theta$ for radial, latitudinal, and longitudinal directions, respectively. The source term S contains the gravitational, centrifugal, and Coriolis forces and the energy source due to these forces. The longitudinal angular size $\Delta\phi$ is set equal to $\Delta\theta$, and one longitudinal layer is simulated in this two-dimensional simulation study.

To deal with the large gradient near the inner boundary surface due to the gravity of the Sun and preserve the conservative quantities, we used a set of normalized conservative variables

$$(r^2\varrho, r^2\varrho V_r, r^2\varrho V_{\theta}, r^2\varrho V_{\phi}, rB_r, rB_{\theta}, rB_{\phi}, r^2\mathcal{E}). \quad (8)$$

Note that this normalization does not affect the variables with the dimension of speed such as \mathbf{V} and $\mathbf{B}\varrho^{-1/2}$. The MUSCL

method is used to raise the order of spatial accuracy for the characteristic equations. For the interpolation along the radial direction with varying grid sizes, for example, we used the simple adjustment

$$\begin{aligned}\Delta'U_{i-1/2} &= \Delta U_{i-1/2} \frac{\Delta r_{i+1/2}}{\Delta r_{i-1/2}}, \\ \Delta'U_{i+3/2} &= \Delta U_{i+3/2} \frac{\Delta r_{i+1/2}}{\Delta r_{i+3/2}}\end{aligned}\quad (9)$$

and then interpolated the values on the cell boundary at $r_{i+1/2}$:

$$U_{i+1/2}^l = U_i + \frac{1}{2} \mathbf{R}_i \text{ff}(\mathbf{L}_i \Delta U_{i+1/2}, \mathbf{L}_i \Delta'U_{i-1/2}), \quad (10)$$

$$U_{i+1/2}^r = U_{i+1} - \frac{1}{2} \mathbf{R}_{i+1} \text{ff}(\mathbf{L}_{i+1} \Delta U_{i+1/2}, \mathbf{L}_{i+1} \Delta'U_{i+3/2}), \quad (11)$$

where the subscript i refers to the grid address along the r -direction and \mathbf{L} and \mathbf{R} are the matrix forms of the left and right eigenvectors of the Jacobian matrix $\mathbf{J}(=\partial\mathbf{F}/\partial\mathbf{U})$, respectively. These two matrices are normalized so that $\mathbf{L}\mathbf{R} = \mathbf{R}\mathbf{L} = \mathbf{I}$ (Roe & Balsara 1996; Cargo & Gallice 1997). The matrix \mathbf{L} is given in Appendix B. The interpolations with equations (10) and (11) are of third-order spatial accuracy with the flux-limiting function, $\text{ff}(\dots, \dots)$,

$$\text{ff}(a, b) = \frac{1-\kappa}{2} \text{minmod}(a, \omega b) + \frac{1+\kappa}{2} \text{minmod}(b, \omega a), \quad (12)$$

and the $\text{minmod}(\dots, \dots)$ function,

$$\text{minmod}(x, y) = \begin{cases} \text{sgn}(x) \min(|x|, |y|), & xy > 0, \\ 0, & \text{otherwise,} \end{cases} \quad (13)$$

where $\kappa = 1/3$ and $\omega = (3 - \kappa)/(1 - \kappa)$. While the adjustment with equation (9) is insufficient, we confirmed that this worked well in conjunction with equation (12). Finally, the numerical flux at the cell interface, $\mathbf{F}_{r; i+1/2}^*$, is evaluated in accordance with the TVD method:

$$\begin{aligned}\mathbf{F}_{r; i+1/2}^* &= \frac{\mathbf{F}_r(U_{i+1/2}^r) + \mathbf{F}_r(U_{i+1/2}^l)}{2} \\ &\quad - \frac{1}{2} \mathbf{R} |\mathbf{A}| \mathbf{L} (U_{i+1/2}^r - U_{i+1/2}^l),\end{aligned}\quad (14)$$

where the matrix $|\mathbf{A}|$ is $\text{diag}(|\lambda_1|, \dots, |\lambda_7|)$ and all matrices \mathbf{L} , \mathbf{R} , and $|\mathbf{A}|$ are evaluated with Roe's average of U^r and U^l (Roe 1981). Our code is dimensionally unsplit, and the numerical flux on the cell interface in the latitudinal direction, \mathbf{F}_θ^* , is obtained in the same manner.

The two-step explicit method we used to trace the temporal evolution of the MHD variables can be written as

$$U^p = U^n + \frac{\Delta t}{2} \text{RHS}(U^n), \quad (15)$$

$$U^{n+1} = U^n + \Delta t \text{RHS}(U^p), \quad (16)$$

where the superscripts n, p , and $n+1$ refer to the known state at the n th time step, the provisional state at the intermediate time

step, and the updated state, respectively. The time increment step Δt is determined with the Courant-Friedrichs-Lewy (CFL) condition (eq. [A6]).

2.3. Treatment of $\nabla \cdot \mathbf{B}$

The treatment of the nonzero divergence of the magnetic field, $\nabla \cdot \mathbf{B}$, is important for the numerical stability and accuracy in multidimensional MHD simulations. One orthodox strategy is to employ the vector potential presentation, $\mathbf{B} = \nabla \times \mathbf{A}$, which automatically guarantees a divergence-free magnetic field. In this method, the governing equations have second-order spatial derivatives of \mathbf{A} that may make boundary treatments complicated. The constraint transportation (CT) method (Evans & Hawley 1988; Tóth 2000) is another powerful technique to suppress the emergence of nonzero divergence of the magnetic field. However, with this method the initial small nonzero $\nabla \cdot \mathbf{B}$ may remain all through the computation. Because of these reasons, in this paper, we used two other methods to reduce the nonphysical effects of $\nabla \cdot \mathbf{B}$.

The first is the Powell correction, where the artificial terms $-\mathbf{V}(\nabla \cdot \mathbf{B})$, $-\mathbf{B}(\nabla \cdot \mathbf{B})$, and $-(\mathbf{V} \cdot \mathbf{B})(\nabla \cdot \mathbf{B})$ are added to the right side of the induction, momentum, and energy equations, respectively (Brackbill & Barnes 1980; Powell 1994). The artificial term added to the induction equation works to clean up $\nabla \cdot \mathbf{B}$ effectively in coronal holes and interplanetary space. This can be understood by seeing the equation

$$\left(\frac{\partial}{\partial t} + \mathbf{V} \cdot \nabla\right) \left(\frac{\nabla \cdot \mathbf{B}}{\rho}\right) = 0 \quad (17)$$

that is obtained by coupling the modified induction equation (4) and the continuity equation (2). Because this equation means that the numerical monopole $\nabla \cdot \mathbf{B}$ will move together with the plasma, $\nabla \cdot \mathbf{B}$ in the region where the plasma has substantial flow speed will be swept away. The other added terms work to cancel the nonphysical forces due to nonzero $\nabla \cdot \mathbf{B}$ in the entire computational domain.

The other method solves the Poisson equation,

$$\nabla \cdot (\nabla \Psi_m) + \nabla \cdot \mathbf{B} = 0, \quad (18)$$

and then replaces the magnetic field

$$\mathbf{B}' = \mathbf{B} + \nabla \Psi_m \quad (19)$$

at every time step (Schmidt-Voigt 1989; Tanaka 1995). This procedure can remove the magnetic monopole completely. However, it is expensive in computation. Thus, instead of solving fully, our code calculates several or 10 iteration steps of the relaxation equation

$$\frac{\partial \Psi_m'}{\partial t'} = \nabla \cdot (\nabla \Psi_m') + \nabla \cdot \mathbf{B} \quad (20)$$

with the time increment step $\Delta t' (< \Delta t)$. Although the value of Ψ_m' obtained in this way does not satisfy equation (18) and thus the numerical monopole cannot be fully removed, the replacement of the magnetic field with

$$\mathbf{B}' = \mathbf{B} + \nabla \Psi_m' \quad (21)$$

TABLE 1
BOUNDARY CONSTRAINTS

| Label (1) | Provisional NV_r (2) | Constraints (3) | Equation (4) |
|--------------|---------------------------|---|-----------------|
| BC0 | Any values | $\partial_r B_r = 0, (\mathbf{V} \times \mathbf{B})_{\theta, \phi} = 0$ | ... |
| BC1 | $0 < NV_r < (NV_r)_c$ | $\partial_r N = 0, \partial_r P_g = 0$ | B28 |
| BC2 | $NV_r < 0$ | $\mathbf{V} = \mathbf{0}, \partial_t(P_g/N^{1.05}) = 0$ | B33 |
| BC3a | $NV_r > (NV_r)_c$ | $NV_r = (NV_r)_c, \partial_t(P_g/N) = 0$ | B41 |
| BC3b | $NV_r > (NV_r)_c$ | $NV_r = (NV_r)_c, \partial_r N = 0$ | B42 |
| BC3ab | $NV_r > (NV_r)_c$ | $NV_r = (NV_r)_c, \partial_t(P_g/N^{5/3}) = 0$ | B41 |
| BC3ab' | $NV_r > (NV_r)_c$ | $NV_r = (NV_r)_c, \partial_t(P_g/N^{1.05}) = 0$ | B41 |

NOTES.—Columns, from left to right: (1) the labels of the boundary constraints; (2) the mass flux provisionally calculated with BC1; (3) the given constraints; and (4) the characteristic equations to be solved. The boundary constraint BC0 (eqs. [B20], [B22], and [B23]) is used to construct all characteristic equations (eqs. [B28], [B33], [B41], and [B42]).

can reduce the residual divergence of the magnetic field to a sufficiently small size until the time relaxation of the MHD equation can be completed. By using both the Powell correction and the replacement procedure with equation (21), the divergence of the magnetic field in both coronal hole regions and streamers can be reduced sufficiently.

3. TREATMENTS OF THE BOUNDARY SURFACE

To determine variables on the outer boundary surface at $300 R_\odot$, we employed a linear extrapolation. Because the solar wind there is always supersonic/Alfvénic, this treatment is equivalent to a nonreflecting boundary.

On the contrary, the treatment at the sub-Alfvénic solar surface (at $1.01 R_\odot$) must be determined carefully at each location, because we have to consider the nonlinear MHD interactions between the solar surface and solar corona. The boundary treatment we examined is based on the projected normal characteristic method proposed by Nakagawa (1980) and practically used by Wu & Wang (1987). Here only some basic aspects of our treatments are described. The detailed formulation is presented in Appendix B.

The projected normal characteristic method uses the information of only the outgoing MHD waves to update the MHD variables on the boundary surface because we have no information about the incoming MHD waves. To compensate for the lack of information and complete the equation system, we must provide the same number of constraints as the incoming MHD waves. While some arbitrary choices are allowed when determining the constraints, the constraints should be determined in a manner such that the assumptions can reasonably describe the situation to be simulated.

In this simulation we assume that the radial component of the plasma flow velocity, V_r , is always outward and less than the slow MHD wave, $0 \leq V_r < V_{S,r}$ ($V_{S,r}$ is defined in eq. [A4]), in order to avoid increasing the number of choices of the boundary treatment and for simplicity. The non-negativity is enforced by the boundary treatment shown later, and whether $V_r \leq V_{S,r}$ is monitored during the simulation. In this case, three of the eight MHD wave velocities (λ_1, λ_2 , and λ_3 in eq. [A1]) are always negative at all computational grid points on the solar surface at all time steps. Thus, there are always three outgoing and five incoming MHD waves on the inner boundary. Therefore, in this study, the number of constraints to be determined is five.

First, we assume that the radial component of the solar surface magnetic field is fixed, because we are going to obtain the quiet solar wind matching the specified solar surface magnetic

field. This assumption yields three constraints (eqs. [B20], [B22], and [B23]; Yeh & Dryer 1985). As mentioned in § B1, these three constraints are necessary to keep the magnetic solenoidality. Therefore, we have to always use these three constraints, which are hereafter labeled BC0.

Two constraints remain to be determined. As mentioned, our boundary model explicitly limits the solar surface local mass flux to obtain the appropriate solar wind mass flux at the outer boundary. In addition, we have assumed that $V_r \geq 0$. Therefore, the remaining two boundary constraints are determined in accordance with the solar surface mass flux or flow speed. We will hereafter use the proton number flux NV_r , and the constraints will be made for three cases: BC1, low-mass flux when $0 < NV_r < (NV_r)_c$; BC2, no mass flux when $NV_r = V_r = 0$; and BC3, mass flux limited when $NV_r > (NV_r)_c$. In the limited mass flux case, BC3, the model can adjust by altering the density, the temperature, or both. The average number flux estimated from *Ulysses* data (eq. [1]), $8.0 \times 10^8 \text{ km s}^{-1} \text{ cm}^{-3}$, is used as the critical number flux $(NV_r)_c$. In order to construct the constraints, we made the straightforward assumptions described in the following sections and tabulated in Table 1.

3.1. Boundary Constraint BC1: Fixed Temperature and Density for Low-Mass Flux

Wherever $0 < NV_r < (NV_r)_c$, we assume that the density and temperature are fixed. That is, the transition region beneath the inner simulation boundary supplies the same amount of plasma and thermal energy as escapes from the Sun when the mass flux is at a moderate level. The temporal variations of the other variables are calculated with the characteristic equation (B28) so that the derived temporal variations on the solar surface will match the governing hyperbolic MHD system.

It should be noted here that when the magnetic field, \mathbf{B} , and the solar rotation, $\boldsymbol{\Omega}$, are set to zero, the simulated plasma should be identical to the Parker solution and only BC1 should be used. The experimental simulation with $\mathbf{B} = \boldsymbol{\Omega} = 0$ confirms that the differences between the simulated solution and the analytical Parker solution are less than 0.5%. Thus, the boundary treatment BC1 that can adjust the solar surface flow speed works well in this hydrodynamic case.

On the other hand, with a magnetic field present, the updated values of NV_r can vary significantly and become less than zero or greater than $(NV_r)_c$. In practice, our simulation code first calculates the temporal evolution of NV_r with this boundary treatment, and then it checks whether the provisionally updated NV_r remain between zero and $(NV_r)_c$. If the updated NV_r is outside

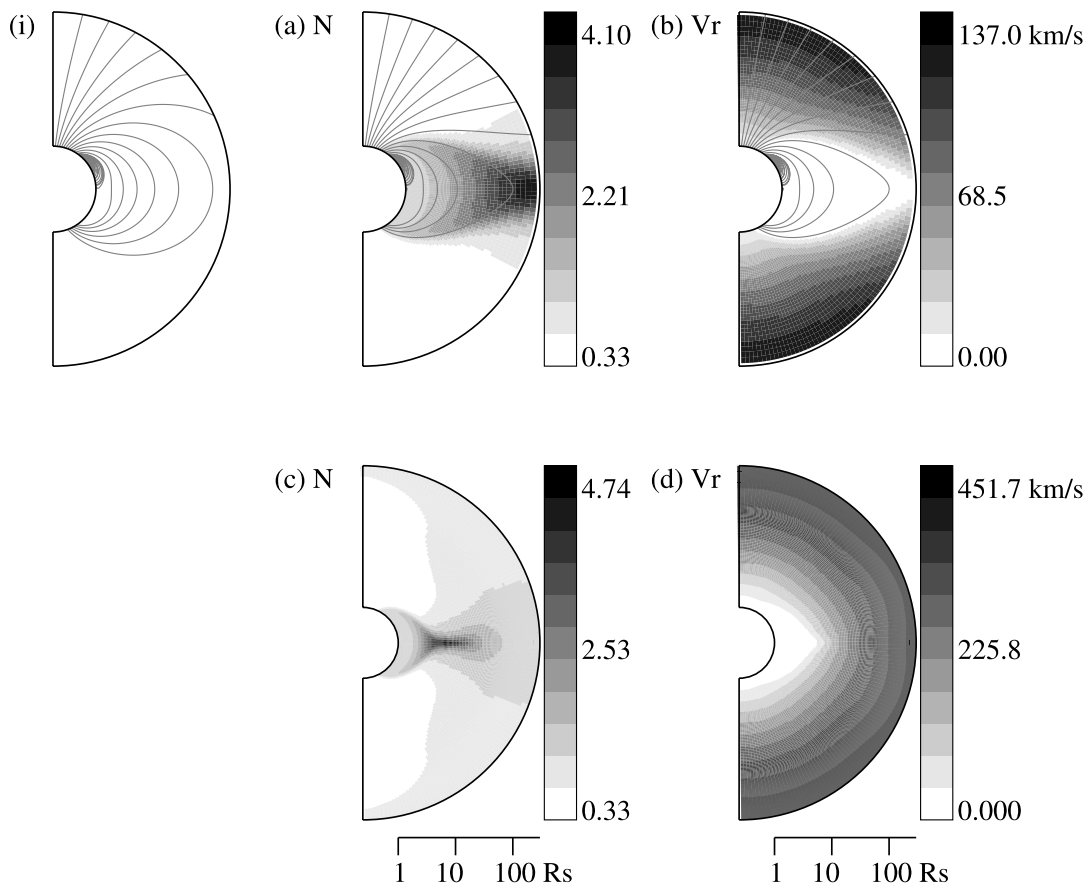


FIG. 1.—Density contrast, radial component of the plasma flow, and magnetic field lines for heliocentric altitudes from 1.01 to $4.2 R_{\odot}$ (top) and to $300 R_{\odot}$ (bottom) obtained with case A (uniform temperature at the base of the coronal hole). The gray scales of (a) and (c) are the ratio to the average at each height to show the density contrast in the steady solution of the solar wind. The gray scales of (b) and (d) show the radial component of the solar wind flow velocity, V_r . The magnetic field lines in the simulated steady corona are drawn in (a) and (b), and the initial magnetic field lines are drawn in (i). Only the field lines starting in the northern hemisphere are drawn for clarity. The field is axisymmetric.

of this range, the temporal evolution is recalculated with BC2 or BC3.

3.2. Boundary Constraint BC2: Polytrope Law for Stagnant Plasma in Closed Field Regions

Wherever the provisionally updated NV_r is less than 0 and the plasma flow is outward, NV_r is reset to zero and the density and gas pressure will adjust to maintain the polytropic relation (eqs. [B29]). This case generally occurs in closed field regions near the solar equator where the solar coronal plasma is stagnant.

This assumption means that the inner boundary surface acts like a wall, such that plasma falling from the corona will stagnate on the surface. In the simulation, we examined the density and pressure increase slightly to reach a hydrostatic state. This is associated with a slight corresponding increase of the horizontal component of the magnetic field due to the precipitation of the confined plasma at the first phase of the time-relaxation simulation.

3.3. Boundary Constraint BC3 (BC3a, BC3b, and BC3ab): Limited Mass Flux and Variable Temperature and Density at Coronal Hole Regions

Wherever the mass flux exceeds the critical value, $NV_r > (NV_r)_c$, NV_r is reset to $(NV_r)_c$ so that the solar wind mass flux will match the *Ulysses* measurements (eq. [B34]). Because the

mass flux is fixed at the critical value, the density and temperature will decrease due to the shortage of mass and thermal energy supplied from the transition region. To express the decrease of density and temperature, we assume that the polytropic gas is represented by the surface specific heat ratio, γ' (eq. [B38]). Note that γ' does not have to be the same as the γ appearing in the basic equations (2)–(5) because the solar wind plasma comes from outside the computational domain.

We examined four cases with different values of γ' . The first one (hereafter BC3a) is the fixed temperature condition with $\gamma' = 1$ (eq. [B36]), the second one (hereafter BC3b) is the fixed density condition $\gamma' = +\infty$ (eq. [B37]), and the last two are made with $\gamma' = 5/3$ and 1.05 as the intermediate choice between BC3a and BC3b (thus labeled BC3ab and BC3ab').

Boundary constraint BC3a allows the surface mass density to change. In this simulation, the plasma density at the coronal hole base decreases so that the kinetic energy $[\sim(NV_r)_c^2/2N]$ and flow speed $[(NV_r)_c/N]$ reach equilibrium with the fixed temperature and the given surface magnetic field distribution.

With the constraint BC3b, the temperature in the open-field regions decreases until the system reaches equilibrium with the fixed density, mass flux (and thus the radial component of the plasma flow velocity), and the given surface magnetic field. Therefore, the simulation results with BC3a (BC3b) can be expected to have the good contrasts of the density (the temperature) on the inner boundary surface and in the solar corona.

TABLE 2
THE BOUNDARY CONSTRAINTS FOR EACH CASE

| CASE (1) | BOUNDARY TREATMENT | | | FIGURE (5) |
|-------------|----------------------|------------------------------|--------------------------------------|---------------|
| | $NV_r \leq 0$ (2) | $0 < NV_r < (NV_r)_c$ (3) | $NV_r \geq (NV_r)_c$ (4) | |
| A..... | BC0 and BC2 | BC0 and BC1 | BC0 and BC3a (uniform N) | 2 |
| B..... | BC0 and BC2 | BC0 and BC1 | BC0 and BC3b (uniform T) | 3 |
| O..... | BC0 and BC2 | BC0 and BC1 | BC0 and BC1 (uniform N and T) | 4 |
| AB..... | BC0 and BC2 | BC0 and BC1 | BC0 and BC3ab (linked N and T) | 5 |
| AB'..... | BC0 and BC2 | BC0 and BC1 | BC0 and BC3ab' (linked N and T) | 6 |

NOTES.—Columns, from left to right: (1) the case; (2–4) the boundary treatments used when provisionally calculated mass flux is outgoing, incoming and lower than critical value, or higher than critical value; (5) the corresponding figure number. The provisional mass flux is calculated with BC1.

With the intermediate constraint, BC3ab, contrast of both temperature and density will be obtained.

4. SIMULATION AND RESULTS

To impose the two-dimensional distribution of the solar surface magnetic field at the minimum phase of solar activity, we used the dipole and quadrupole components of the solar magnetic field. We used the synoptic photospheric field from the Wilcox Solar Observatory (WSO) at Stanford University (Hoeksema & Scherrer 1986) in 1995 April (Carrington rotation 1894). To avoid prescribing the magnetic field topology of the open/closed structure, in this study, we used a potential field-

source surface model (Schatten et al. 1969) with the source surface located at infinity. Therefore, the initial magnetic field has only the closed structure (see Fig. 1). This initial field strength was multiplied by the factor of 1.8 that is based on the WSO calibration analysis by Svalgaard et al. (1978). The analytic solutions of the spherically symmetric steady flow (Parker 1958) are given as the initial values of the plasma density, ρ , temperature, T (or gas pressure P_g), and the radial component of the plasma velocity, V_r . The initial solar surface temperature and number density are set to be 1.47 MK and $2.0 \times 10^8 \text{ cm}^{-3}$, respectively. The two transverse components of the initial plasma velocity, V_θ and V_ϕ , are set to zero. On the solar surface

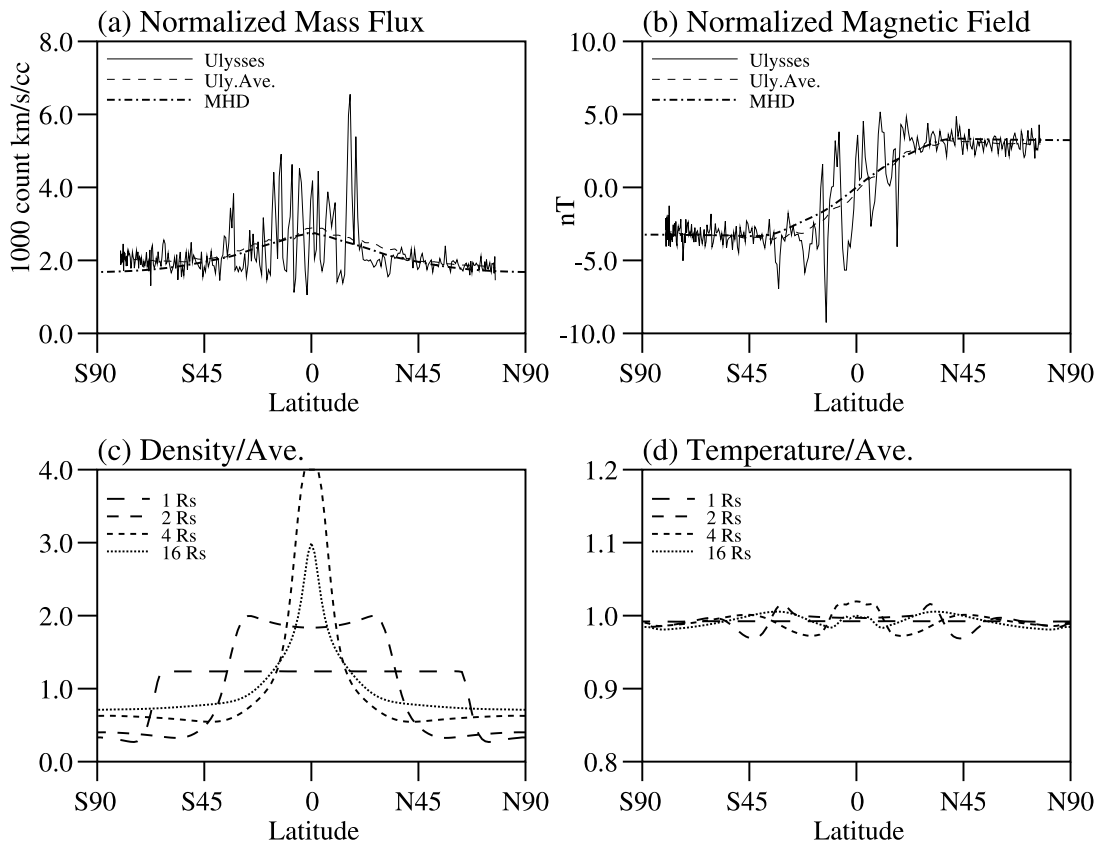


FIG. 2.—Latitudinal distributions of the solar wind simulated for case A (BC0, BC1, BC2, and BC3a), where the temperature at the base of the coronal hole is uniform. Panel (a) shows the mass flux of the simulated solar wind sampled at the measurement positions of the *Ulysses* (dash-dotted line) and the daily and 27 day average of the *Ulysses* measurement (solid and dashed line). Panel (b) shows the radial component of the magnetic field in the same manner. Both *Ulysses* data and the simulated solar wind parameters drawn in (a) and (b) are normalized to 1 AU, assuming $NV_r r^2$ and $B_r r^2$ are preserved. Panels (c) and (d) show the latitudinal distribution of the relative density and temperature at various heliocentric distances (1, 2, 4, and 16 R_\odot), which are divided by the average at each heliocentric distance.

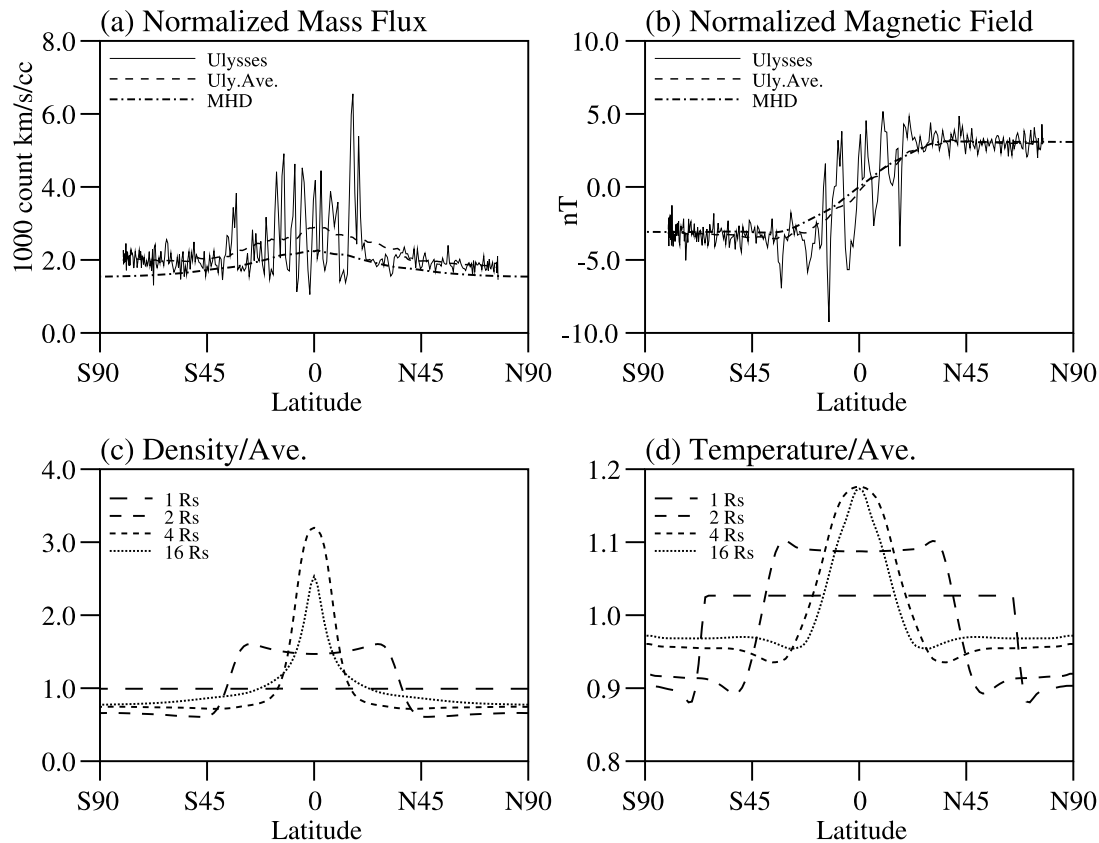


FIG. 3.—Latitudinal distributions of the solar wind simulated for case B (BC0, BC1, BC2, and BC3b), where the density at the base of the coronal hole is uniform. Plots are made in a manner identical to Fig. 2.

boundary the initial plasma flow is defined as $V \propto \mathbf{B} \cdot \mathbf{B}_r / B^2$ so that the plasma flow is parallel to the magnetic field (eqs. [B22] and [B23] in Appendix B).

We carried out MHD simulations to examine the new boundary constraints BC3a, BC3b, BC3ab, and BC3ab' for $NV_r > (NV_r)_c$. For reference, the simulation using BC1 for $NV_r > (NV_r)_c$ was also tested. The simulations with the choices above are labeled case A, case B, case AB, case AB', and case O. Table 2 summarizes the boundary constraints used in each choice.

The simulated solar corona and solar wind reach a quasi-steady state after a time-relaxation MHD simulation of about 200 hr in real time. Figure 1 shows the meridional section views of the density, flow speed, and magnetic field lines of the steady solar wind obtained with case A. The total area of the open-field region is about 13% of the entire solar surface. This simulation of the solar wind undergoes more rapid expansion of solar coronal magnetic flux than a purely dipole field because of the presence of the small bipolar structure at the middle latitude regions. In the closed field region near the solar equator where the plasma is stagnant, a small plasma motion remains. However, the residual flow speed was about $0.01\text{--}0.1 \text{ km s}^{-1}$ or less than $1/10,000$ of the local magneto-acoustic wave speed. Thus, we consider the solar wind solution to be steady state.

Comparison with *Ulysses* measurements covering a wide range of heliographic latitude is a good benchmark to check the latitudinal distribution of the simulated distant solar wind originating the solar surface on which the boundary treatments are made. Figures 2, 3, 4, 5, and 6 show the latitudinal distribution of the simulated solar wind. Because the simulations were done in two dimensions using an axisymmetric solar mag-

netic field, the results represent the features averaged over longitude. We therefore prepared 27 day averages of *Ulysses* data for comparison.

Panel (a) in each figure shows the latitudinal distribution of the solar wind mass flux sampled at the latitudes of *Ulysses* measurements; superimposed are the daily and 27 day average of the *Ulysses* data. Panel (b) shows the radial component of the magnetic field in the same manner as panel (a). For this comparison, we used the data set from the Coordinated Heliospheric Observations (COHO) Web database at NSSDC of NASA. The averages of these quantities are also tabulated in Table 3. Panels (c) and (d) show the relative density and temperature at various heliocentric distances normalized with the average at each distances.

In the comparison of the mass flux and magnetic field in panels (a) and (b), good agreement between the simulated and measured parameters is obtained, especially in the high-latitude regions when the mass flux is limited in cases A, B, AB, and AB' (Figs. 2, 3, 5, and 6). The simulated density and magnetic field at the low-latitude region also agree well with the 27 day average of the *Ulysses* measurement. The agreement of the mass flux implies that the boundary constraints are capable of adequately controlling mass flux escaping from the Sun and that some aspects of the latitudinal structure of the solar wind are adequately obtained with this simulation. In addition, the simulated uniform magnetic field in the high-latitude regions is similar in strength to the *Ulysses* measurements; this also supports the adequacy of our boundary treatments.

The mass flux obtained with case O (Fig. 4a) is much higher than that obtained with case A or B. This excess of mass flux is due to the unlimited mass flux on the inner boundary and is

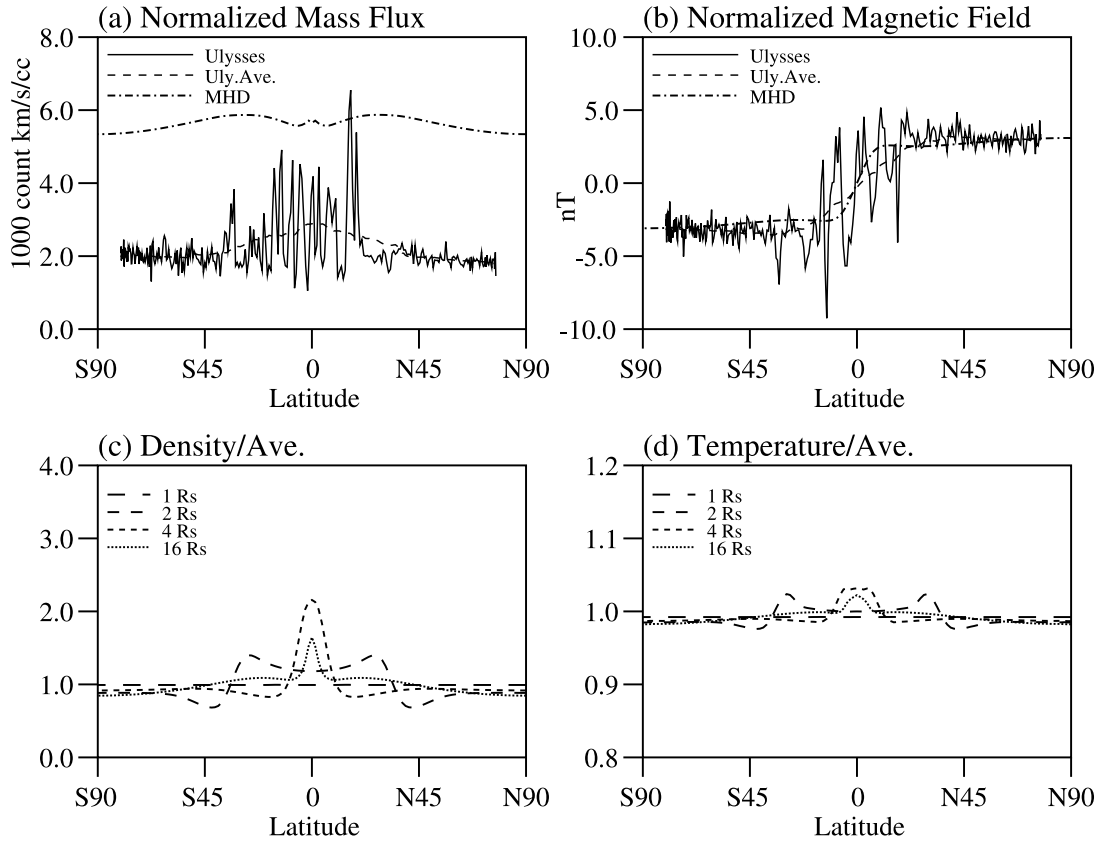


FIG. 4.—Latitudinal distributions of the simulated solar for case O (only BC0, BC1, and BC2), where both density and temperature at the base of the coronal hole are uniform. In this case, the mass flux escaping from the open-field regions is not limited and thus larger. Plots are made in a manner identical to Fig. 2.

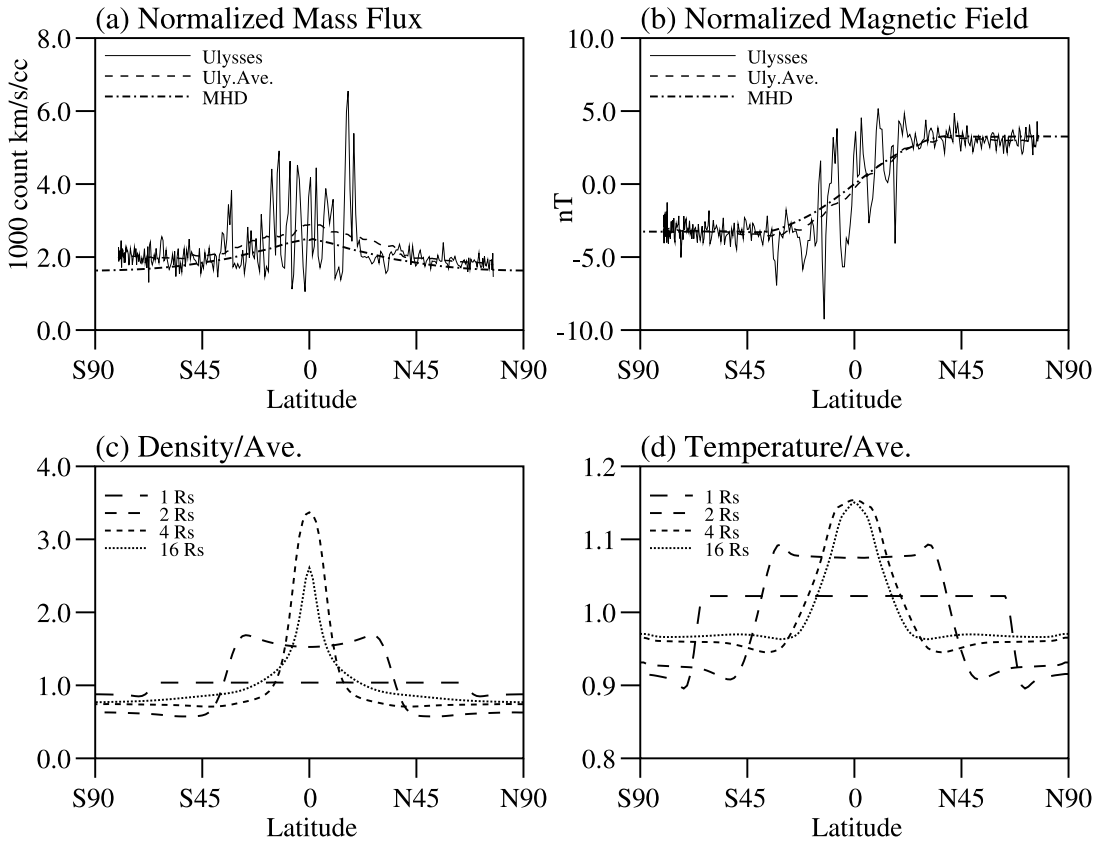


FIG. 5.—Latitudinal distributions of the solar wind simulated for case AB (BC0, BC1, BC2, and BC3ab), with solar surface specific heat ratio γ' equal to 5/3. Plots are made in a manner identical to Fig. 2.

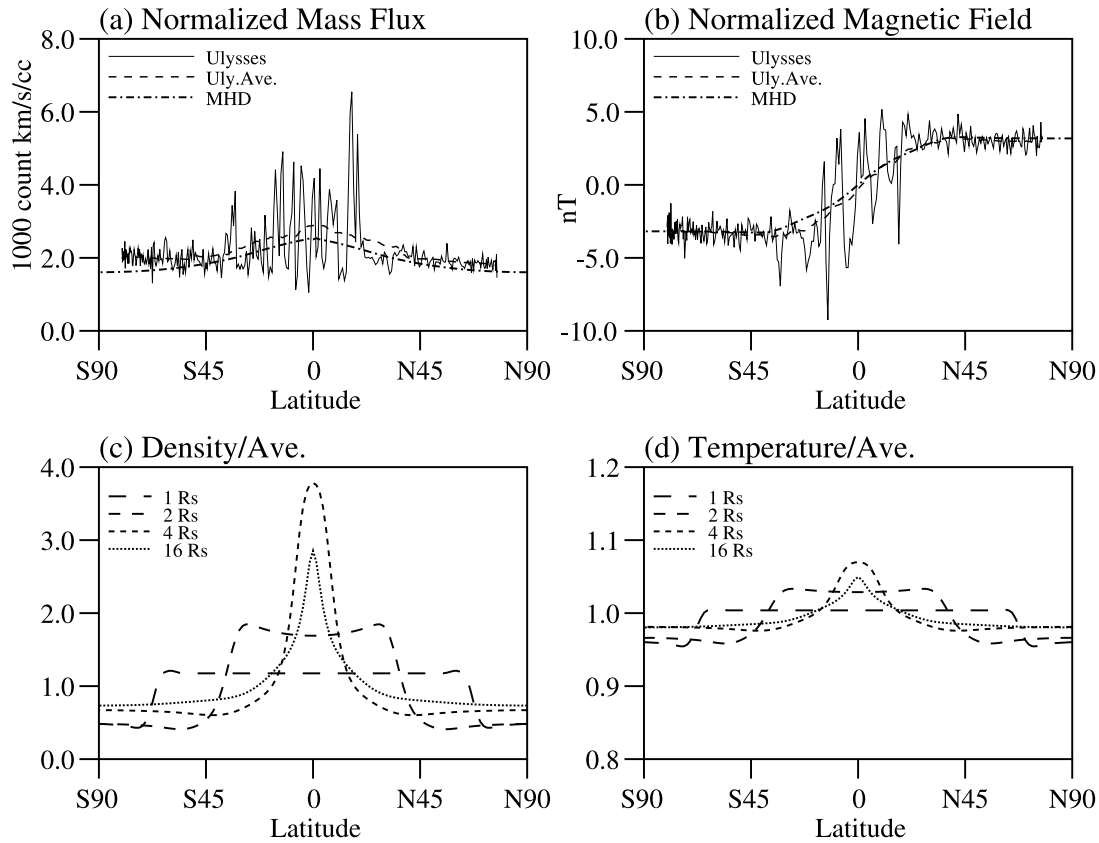


FIG. 6.—Latitudinal distributions of the solar wind simulated for case AB' (BC0, BC1, BC2, and BC3ab'), with solar surface specific heat ratio γ' equal to 1.05. Plots are made in a manner identical to Fig. 2.

responsible for the formation of the latitudinally wider uniform solar wind at the polar region than other cases.

Boundary constraints BC3a and BC3b are chosen to produce significant contrast between the coronal hole and streamer even when the simulation starts with a uniform plasma distribution. The temperature and density at the base of the coronal hole obtained with cases A, B, and others are tabulated in Table 3. Figure 2c shows the density contrast between the streamer and coronal hole obtained with case A. The surface density obtained at the base of the coronal hole is about $5 \times 10^7 \text{ cm}^{-3}$, and the typical ratios of the simulated density in the

coronal hole to that in the streamer are 1:4 at $1.01 R_{\odot}$, 1:6 at $2 R_{\odot}$, and 1:8 at $4 R_{\odot}$. Although the density variation with radial distance may be determined by the conditions on the solar surface and the coronal acceleration mechanism, the contrast obtained with our simulation model is consistent with the contrast in the solar corona. The density contrasts obtained with cases B and O (Figs. 3c and 4c) are smaller than that obtained with case A.

Figure 3d shows the temperature contrast obtained with case B. The computed contrast in temperature is about 10% of the average at $1.01 R_{\odot}$. While this computed contrast on the solar

TABLE 3
SOME QUANTITIES OF THE SIMULATED SOLAR WIND

| Case (1) | β_p^{-1} (10^2) (2) | N_p (10^8 cm^{-3}) (3) | T_p (MK) (4) | V_p (km s^{-1}) (5) | $\langle NV_r \rangle$ (1 AU) ($10^3 \text{ km s}^{-1} \text{ cm}^{-3}$) (6) | $\langle B_p \rangle$ (1 AU) (nT) (7) | γ' (Surface) (8) | Figure (9) |
|----------------------|-------------------------------------|--|----------------------|--|--|---|----------------------------|---------------|
| A..... | 4.15 | 0.537 | *1.47 | 14.7 | 2.20 | 3.22 | 1.00 | 2 |
| B..... | 1.27 | *2.00 | 1.29 | 4.00 | 1.88 | 3.06 | $+\infty$ | 3 |
| O..... | *1.11 | *2.00 | *1.47 | 13.5 | 5.68 | 2.76 | ... | 4 |
| AB..... | 1.34 | 1.87 | 1.30 | 4.27 | 1.90 | 3.01 | 5/3 | 5 |
| AB'..... | 2.84 | 0.82 | 1.41 | 9.64 | 2.06 | 3.16 | 1.05 | 6 |
| <i>Ulysses</i> | | | | | 2.34 | 3.10 | | |

NOTES.—Columns, from left to right: (1) the case; (2) the ratio of magnetic pressure to gas pressure, β_p^{-1} , in units of 100; (3) the particle number density; (4) the temperature; (5) the radial component of the flow at the polar region on the solar surface; (6) the average of the mass flux, $\langle NV_r \rangle$; (7) the magnetic field strength, $\langle B_p \rangle$, normalized to 1 AU; (8) γ' , the surface specific heat ratio for the polytrope model used in each choice; (9) the corresponding figure number. The asterisks (*) are attached to the numbers that are the same as the initial values. The value of $\langle B_p \rangle$ is calculated by sampling only heliographic latitudes greater than 30° . The numbers in the bottom row are the corresponding parameters calculated using *Ulysses* data. The numbers in the rightmost column give the figure number illustrating the simulated latitudinal structures.

surface (from 1.35 to 1.5 MK) is smaller than that obtained from the analysis of *Ulysses* data by Geiss et al. (1995; from 1.1 to 1.7 MK), it can be said that BC3b is capable of retrieving some temperature distribution at the base of the corona.

Figures 5c, 5d, 6c, and 6d show the contrasts of the solar coronal plasma obtained with cases AB and AB'. The typical contrast of the density and temperature at $1.01 R_{\odot}$ obtained with case AB (AB') are about 1:1.2 (1:2) and 1:1.1 (1:1.05), respectively. The boundary constraint BC3ab ($\gamma' = 5/3$) is capable of simultaneously producing a temperature contrast similar to that obtained with BC3b ($\gamma' = \infty+$) and the substantial contrast of the density and the constraint BC3ab' ($\gamma' = 1.05$) can simultaneously produce a density contrast comparable with that obtained with BC3a ($\gamma' = 1$) and substantial temperature contrast. The actual solar coronal density and temperature must be determined by the dynamics of the solar surface and the transition region. However, agreements obtained with cases A, B, AB, and AB' show that unknown mechanisms at the transition region can be reasonably represented by the polytropic relationship (eq. [B38]) with $\gamma' \geq 1$.

5. DISCUSSION

We formulated boundary treatments at the subsonic near-solar surface that limits solar wind mass flux in an MHD simulation. The treatments of the solar surface boundary are based on the concept of the projected normal characteristic method. Therefore, the boundary parameters are fully compatible with the outgoing MHD waves and the given constraints. The solar surface mass flux limit is set so that the mass flux at the distant regions will match the *Ulysses* measurements and so that a reasonable contrast of the density and temperature at the corona will be obtained simultaneously. The axisymmetric dipole plus quadrupole components of the observed solar surface magnetic field is given to the two-dimensional version of our simulation code as the initial and boundary values of the magnetic field, so that the simulation results will represent the solar wind at the minimum phase of solar activity. The computed solar wind is compared with the data from *Ulysses* made during its first fast-latitude scan. Good agreement is obtained. At the same time, good contrasts of the coronal plasma between the coronal hole and streamer are obtained.

The surface density and temperature are represented with the polytropic model in the boundary treatment. The solar surface specific heat ratios, $\gamma' = 1, 1.05, 5/3$, and $+\infty$, are tested. These choices of the boundary constraint can be also used for future studies. For example, the first one, BC3a, must be useful when the response of the solar corona to a given temperature at the base of the corona is examined. With the second one, BC3ab', the specific heat ratios in the computational domain ($r > 1.01 R_{\odot}$) and on the inner boundary sphere at $r = 1.01 R_{\odot}$ are

the same and equal to 1.05. Thus, the choice BC3ab' is the fully polytropic case. The third one, BC3ab, assumes that there is no special mechanism at the transition region and that plasma behaves as the usual adiabatic gas. Therefore, this choice will be convenient when some mechanism, such as heat conduction and Alfvén wave decay, is examined. The last one, BC3b, will be helpful when the balance of the thermal energy at the base of the corona or the responses of the solar corona to the given surface density is examined.

The simulations shown in this study were done in two dimensions to simulate the global structure of the solar wind in the solar minimum activity phase. Three-dimensional simulation will be necessary when simulating other phases of the solar cycle with much more complicated magnetic field structure. Note that the projected normal characteristic method and the new feature to limit the solar surface mass flux presented in this paper can be used in the three-dimensional simulation without any modification.

The computational cost of the projected normal characteristic method is greater than using simplified boundary conditions, such as a fixed boundary condition. However, the computation is numerically stable, and the solutions obtained near the sub-Alfvénic boundary have almost no numerical oscillation. This boundary treatment will be useful for general MHD simulations if the simulation region is limited by a sub-Alfvénic physical boundary. In addition, many routines for defining matrices and eigenvalues of the MHD system are almost identical to those used in the TVD and MUSCL, and the integration into existing MHD codes with a linearized Riemann solver will not cost very much.

The model descriptions of the solar wind in this simulation study were rather simple. In particular, we have assumed the polytrope model with the specific heat ratio $\gamma = 1.05$ in this study because this is a good model to obtain trans-Alfvénic solar wind flow and it has been used widely in solar wind simulation studies. However, this near-isothermal model generates a slower solar wind acceleration and thus a slower decrease of density near the Sun. Therefore, coronal heating and acceleration models, such as Alfvén wave decay and microscaled magnetic reconnection, have to be considered for enhancing the simulation model.

The author wishes to thank NSSDC of NASA for the use of their publicly available data set of the spacecraft measurement data of the solar wind distributed at the COHO database. This work is supported in part by the NSF/CISM project under grant ATM-0120950, the NASA/MDI project under grant NAS5-13261, and the DoD/MURI project under grants F005001 and SA3206.

APPENDIX A

EIGENVALUES OF THE MHD SYSTEM

The directions and speed of the MHD waves are equal to the eigenvalues of the Jacobian matrix, $\mathbf{J} = \partial\mathbf{F}/\partial\mathbf{U}$. The eight eigenvalues can be explicitly given in a nondecreasing order, e.g., for the radial direction,

$$\begin{aligned} \lambda_1 &= V_r - V_{F;r}, & \lambda_2 &= V_r - V_{A;r}, & \lambda_3 &= V_r - V_{S;r}, & \lambda_4 &= V_r, \\ \lambda_5 &= V_r + V_{S;r}, & \lambda_6 &= V_r + V_{A;r}, & \lambda_7 &= V_r + V_{F;r}, \end{aligned} \quad (\text{A1})$$

where

$$V_{r;A} = |b_r|, \quad (\text{A2})$$

$$V_{F;r} = \sqrt{\frac{1}{2} \left[a^2 + b^2 + \sqrt{(a^2 + b^2)^2 - 4a^2 b_r^2} \right]}, \quad (\text{A3})$$

$$V_{S;r} = \sqrt{\frac{1}{2} \left[a^2 + b^2 - \sqrt{(a^2 + b^2)^2 - 4a^2 b_r^2} \right]}, \quad (\text{A4})$$

and

$$a = \sqrt{\gamma \frac{P_g}{\varrho}}, \quad b_r = \frac{B_r}{\sqrt{4\pi\varrho}}, \quad b^2 = \frac{B_r^2 + B_\theta^2 + B_\phi^2}{4\pi\varrho}. \quad (\text{A5})$$

The fourth eigenvalue, $\lambda_4 (= V_r)$, represents the two characteristic waves (the advection of B_r and P_g/ϱ^γ). The time increment step Δt in equation (16) is determined with the Courant-Friedrichs-Lewy (CFL) condition,

$$\Delta t = \alpha \min \left(\frac{\Delta r}{\max |\lambda_r|}, \frac{r \Delta \theta}{\max |\lambda_\theta|} \right), \quad (\text{A6})$$

where λ_r and λ_θ represent the characteristic velocities along r and θ . In this study, the CFL number α is set to 0.5 for computational stability.

APPENDIX B

FORMULATION OF SOLAR SURFACE BOUNDARY TREATMENTS

The basic idea of the projected normal characteristic method is that only the information of the outgoing waves should be fully used in the routine to update the variables on the boundary surface. Therefore, the first step of this method is to formulate such MHD waves.

Because the normal vector of the inner boundary surface directs radially, it is convenient to use the vector-matrix form of the MHD equations (2)–(5),

$$\frac{\partial \mathbf{U}}{\partial t} = -\frac{\partial \mathbf{F}}{\partial r} + \mathbf{S}_r = -\frac{\partial \mathbf{F}}{\partial \mathbf{U}} \frac{\partial \mathbf{U}}{\partial r} + \mathbf{S}_r = -\mathbf{J} \frac{\partial \mathbf{U}}{\partial r} + \mathbf{S}_r, \quad (\text{B1})$$

where the vector \mathbf{S}_r contains the rest of the parts, such as the spatial derivatives with respect to the latitudinal direction and source terms. In the hyperbolic MHD system, the Jacobian matrix \mathbf{J} can be expressed as

$$\mathbf{J} = \mathbf{R} \mathbf{\Lambda} \mathbf{L}, \quad (\text{B2})$$

where \mathbf{R} and \mathbf{L} are the matrix form of the normalized right and left eigenvectors of \mathbf{J} , respectively, which satisfy $\mathbf{R} \mathbf{L} = \mathbf{I}$, and $\mathbf{\Lambda} = \text{diag}(\lambda_1, \dots, \lambda_7)$. The matrix \mathbf{L} used here is almost identical to the one used in TVD and MUSCL routines and is given as

$$\mathbf{L} = \begin{bmatrix} L_{11} & L_{12} & \cdots & L_{17} \\ L_{21} & L_{22} & \cdots & L_{27} \\ \vdots & & & \vdots \\ L_{71} & L_{72} & \cdots & L_{77} \end{bmatrix} \equiv \begin{bmatrix} \mathbf{l}_1 \\ \mathbf{l}_2 \\ \vdots \\ \mathbf{l}_7 \end{bmatrix}, \quad (\text{B3})$$

with

$$\mathbf{l}_1 = \left[\psi_{L;F}^-, \frac{\alpha_f (-V_{F;r} - \Gamma V_r)}{2a^2 \varrho}, \frac{+\alpha_s V_{S;r} \beta_\theta D_r - \alpha_f \Gamma V_\theta}{2a^2 \varrho}, \frac{+\alpha_s V_{S;r} \beta_\phi D_r - \alpha_f \Gamma V_\phi}{2a^2 \varrho}, \right. \\ \left. \frac{\alpha_s a \beta_\theta - \alpha_f \Gamma b_\theta}{2a^2 \sqrt{\varrho}}, \frac{\alpha_s a \beta_\phi - \alpha_f \Gamma b_\phi}{2a^2 \sqrt{\varrho}}, \frac{\Gamma \alpha_f}{2a^2 \varrho} \right], \quad (\text{B4})$$

$$\mathbf{l}_2 = \left(\psi_{L;A}^-, 0, -\frac{\beta_\phi D_r}{2\varrho}, +\frac{\beta_\theta D_r}{2\varrho}, -\frac{\beta_\phi}{2\sqrt{\varrho}}, +\frac{\beta_\theta}{2\sqrt{\varrho}}, 0 \right), \quad (\text{B5})$$

$$\mathbf{l}_3 = \left[\psi_{L;S}^-, \frac{\alpha_s(-V_{S;r} - \Gamma V_r)}{2a^2\varrho}, \frac{-\alpha_f V_{F;r}\beta_\theta D_r - \alpha_s \Gamma V_\theta}{2a^2\varrho}, \frac{-\alpha_f V_{F;r}\beta_\phi D_r - \alpha_s \Gamma V_\phi}{2a^2\varrho}, \right. \\ \left. -\frac{\alpha_f a \beta_\theta + \alpha_s \Gamma b_\theta}{2a^2\sqrt{\varrho}}, -\frac{\alpha_f a \beta_\phi + \alpha_s \Gamma b_\phi}{2a^2\sqrt{\varrho}}, \frac{\Gamma \alpha_s}{2a^2\varrho} \right], \quad (\text{B6})$$

$$\mathbf{l}_4 = \left(1 - \frac{\Gamma v^2}{2a^2}, \frac{\Gamma V_r}{a^2}, \frac{\Gamma V_\theta}{a^2}, \frac{\Gamma V_\phi}{a^2}, \frac{\Gamma B_\theta}{a^2}, \frac{\Gamma B_\phi}{a^2}, \frac{1-\gamma}{a^2} \right), \quad (\text{B7})$$

$$\mathbf{l}_5 = \left[\psi_{L;S}^+, \frac{\alpha_s(+V_{S;r} - \Gamma V_r)}{2a^2\varrho}, \frac{+\alpha_f V_{F;r}\beta_\theta D_r - \alpha_s \Gamma V_\theta}{2a^2\varrho}, \frac{+\alpha_f V_{F;r}\beta_\phi D_r - \alpha_s \Gamma V_\phi}{2a^2\varrho}, \right. \\ \left. -\frac{\alpha_f a \beta_\theta + \alpha_s \Gamma b_\theta}{2a^2\sqrt{\varrho}}, -\frac{\alpha_f a \beta_\phi + \alpha_s \Gamma b_\phi}{2a^2\sqrt{\varrho}}, \frac{\Gamma \alpha_s}{2a^2\varrho} \right], \quad (\text{B8})$$

$$\mathbf{l}_6 = \left(\psi_{L;A}^+, 0, +\frac{\beta_\phi D_r}{2\varrho}, -\frac{\beta_\theta D_r}{2\varrho}, -\frac{\beta_\phi}{2\sqrt{\varrho}}, +\frac{\beta_\theta}{2\sqrt{\varrho}}, 0 \right), \quad (\text{B9})$$

$$\mathbf{l}_7 = \left[\psi_{L;F}^+, \frac{\alpha_f(+V_{F;r} - \Gamma V_r)}{2a^2\varrho}, \frac{-\alpha_s V_{S;r}\beta_\theta D_r - \alpha_f \Gamma V_\theta}{2a^2\varrho}, \frac{-\alpha_s V_{S;r}\beta_\phi D_r - \alpha_f \Gamma V_\phi}{2a^2\varrho}, \right. \\ \left. \frac{\alpha_s a \beta_\theta - \alpha_f \Gamma b_\theta}{2a^2\sqrt{\varrho}}, \frac{\alpha_s a \beta_\phi - \alpha_f \Gamma b_\phi}{2a^2\sqrt{\varrho}}, \frac{\Gamma \alpha_f}{2a^2\varrho} \right]. \quad (\text{B10})$$

The auxiliary variables are

$$\Gamma = \gamma - 1, \quad (\text{B11})$$

$$\psi_{L;A}^\pm = \mp \frac{D_r(\beta_\phi V_\theta - \beta_\theta V_\phi)}{2\varrho}, \quad (\text{B12})$$

$$\psi_{L;S}^\pm = \frac{\alpha_s(\Gamma v^2/2 \mp V_{S;r}V_r) \mp \alpha_f V_{F;r}D_r(\beta_\theta V_\theta + \beta_\phi V_\phi)}{2a^2\varrho}, \quad (\text{B13})$$

$$\psi_{L;F}^\pm = \frac{\alpha_f(\Gamma v^2/2 \mp V_{F;r}V_r) \pm \alpha_s V_{S;r}D_r(\beta_\theta V_\theta + \beta_\phi V_\phi)}{2a^2\varrho}, \quad (\text{B14})$$

and

$$D_r = \text{sgn } B_r, \quad \alpha_f = \frac{\sqrt{a^2 - V_{S;r}^2}}{\sqrt{V_{F;r}^2 - V_{S;r}^2}}, \quad \alpha_s = \frac{\sqrt{V_{F;r}^2 - a^2}}{\sqrt{V_{F;r}^2 - V_{S;r}^2}}, \quad \beta_{\theta,\phi} = \frac{B_{\theta,\phi}}{\sqrt{B_\theta^2 + B_\phi^2}}. \quad (\text{B15})$$

By operating the matrix \mathbf{L} from the left, equation (B1) becomes

$$\mathbf{L} \frac{\partial \mathbf{U}}{\partial t} = \mathbf{L} \left(-\mathbf{R}\mathbf{A}\mathbf{L} \frac{\partial \mathbf{U}}{\partial r} + \mathbf{S}_r \right) = -\mathbf{A}\mathbf{L} \frac{\partial \mathbf{U}}{\partial r} + \mathbf{L}\mathbf{S}_r. \quad (\text{B16})$$

The l th row of equation (B16),

$$L_{l1} \left(\frac{\partial}{\partial t} + \lambda_l \frac{\partial}{\partial r} \right) \varrho + L_{l2} \left(\frac{\partial}{\partial t} + \lambda_l \frac{\partial}{\partial r} \right) (\varrho V_r) + \dots + L_{l7} \left(\frac{\partial}{\partial t} + \lambda_l \frac{\partial}{\partial r} \right) \mathcal{E} = \sum_{m=1}^7 L_{lm} S_{r,m}, \quad (\text{B17})$$

is an equation of characteristics representing the MHD wave mode whose velocity with respect to r is equal to λ_l .

When $0 \leq V_r \leq V_{S;r}$, three eigenvalues (λ_1 , λ_2 , and λ_3) are always negative. In this case, we can use only three characteristic equations (eq. [B17]) with $l = 1, 2$, and 3 , and the other four characteristic equations can be discarded because they represent incoming MHD waves and do not have any reasonable information in physics. Hereafter, we will use another form of equation (B17),

$$L_{l1} \frac{\partial \varrho}{\partial t} + L_{l2} \frac{\partial (\varrho V_r)}{\partial t} + L_{l3} \frac{\partial (\varrho V_\theta)}{\partial t} + L_{l4} \frac{\partial (\varrho V_\phi)}{\partial t} + L_{l5} \frac{\partial B_\theta}{\partial t} + L_{l6} \frac{\partial B_\phi}{\partial t} + L_{l7} \frac{\partial \mathcal{E}}{\partial t} = \text{RHS}_l, \quad (\text{B18})$$

with

$$\text{RHS}_l = \sum_{m=1}^7 L_{lm} \text{RHS}_m. \quad (\text{B19})$$

To determine all seven temporal variations, $\partial \varrho / \partial t, \dots, \partial \mathcal{E} / \partial t$, four constraints must be given so that equation (B18) is determinable. In this study, the constraints can be expressed in terms of the relationship among the temporal variations.

B1. COMMON BOUNDARY CONSTRAINT, BC0

The temporal evolution of the magnetic field normal to the boundary surface, $\partial B_r / \partial t$, can be separated from the characteristic system, and therefore it does not appear in equation (B18). In this simulation study where the steady state of the coronal structures with the specified distribution of the solar surface magnetic field are to be obtained, the fixed condition,

$$\frac{\partial B_r}{\partial t} = 0, \quad (\text{B20})$$

is used. Yeh & Dryer (1985) pointed out that a constraint,

$$\left. \frac{\partial B_r}{\partial t} - \nabla \times (\mathbf{V} \times \mathbf{B}) \right|_r = 0, \quad (\text{B21})$$

should be satisfied on the boundary surface so that the sinusoidal condition, $\nabla \cdot \mathbf{B} = 0$, will be preserved. To satisfy equations (B20) and (B21), we employed simple straightforward conditions:

$$(\nabla \times \mathbf{B})_\theta = V_\phi B_r - V_r B_\phi = 0, \quad (\text{B22})$$

$$(\nabla \times \mathbf{B})_\phi = V_r B_\theta - V_\theta B_r = 0. \quad (\text{B23})$$

These two yield two constraints expressed in terms of temporal derivatives,

$$V_r \frac{\partial B_\theta}{\partial t} + B_\theta \frac{\partial V_r}{\partial t} - B_r \frac{\partial V_\theta}{\partial t} = 0, \quad V_r \frac{\partial B_\phi}{\partial t} + B_\phi \frac{\partial V_r}{\partial t} - B_r \frac{\partial V_\phi}{\partial t} = 0, \quad (\text{B24})$$

or

$$\varrho V_r \frac{\partial B_\theta}{\partial t} + B_\theta \frac{\partial (\varrho V_r)}{\partial t} - B_r \frac{\partial (\varrho V_\theta)}{\partial t} = 0, \quad \varrho V_r \frac{\partial B_\phi}{\partial t} + B_\phi \frac{\partial (\varrho V_r)}{\partial t} - B_r \frac{\partial (\varrho V_\phi)}{\partial t} = 0. \quad (\text{B25})$$

In this study, three constraints, equations (B20) and (B25), are always employed and labeled BC0. Note that the temporal variations of B_θ and B_ϕ do not have to be zero and thus the inclination angle of the solar surface magnetic field can vary.

B2. BOUNDARY CONSTRAINT FOR $0 < NV_r < (NV_r)_c$, BC1

For the case $0 < NV_r < (NV_r)_c$, we assume that the plasma density and pressure do not change:

$$\frac{\partial \varrho}{\partial t} = 0, \quad \frac{\partial P}{\partial t} = 0. \quad (\text{B26})$$

Then, with equations (B20), (B25), and (B26), the temporal variation of the energy can be written in terms of the temporal derivatives of other variables:

$$\begin{aligned} \frac{\partial \mathcal{E}}{\partial t} &= \mathbf{V} \cdot \frac{\partial (\varrho \mathbf{V})}{\partial t} + \mathbf{B} \cdot \frac{\partial \mathbf{B}}{\partial t} \\ &= \frac{V_r B^2}{B_r^2} \frac{\partial (\varrho V_r)}{\partial t} + \left(\frac{\varrho V_r V_\theta}{B_r} + B_\theta \right) \frac{\partial B_\theta}{\partial t} + \left(\frac{\varrho V_r V_\phi}{B_r} + B_\phi \right) \frac{\partial B_\phi}{\partial t}. \end{aligned} \quad (\text{B27})$$

Finally, putting equations (B25) and (B27) to equation (B18), we obtain the relationships among the temporal variations $\partial (\varrho V_r) / \partial t$, $\partial B_\theta / \partial t$, and $\partial B_\phi / \partial t$:

$$\begin{aligned} &\left(L_{l2} + L_{l3} \frac{B_\theta}{B_r} + L_{l4} \frac{B_\phi}{B_r} + L_{l7} \frac{V_r B^2}{B_r^2} \right) \frac{\partial (\varrho V_r)}{\partial t} \\ &+ \left[L_{l3} \frac{\varrho V_r}{B_r} + L_{l5} + L_{l7} \left(\frac{\varrho V_r V_\theta}{B_r} + B_\theta \right) \right] \frac{\partial B_\theta}{\partial t} \\ &+ \left[L_{l4} \frac{\varrho V_r}{B_r} + L_{l6} + L_{l7} \left(\frac{\varrho V_r V_\phi}{B_r} + B_\phi \right) \right] \frac{\partial B_\phi}{\partial t} = \text{RHS}_l. \end{aligned} \quad (\text{B28})$$

This is a set of three equations ($l = 1, 2,$ and 3), and the temporal variations of ϱV_r , B_θ , and B_ϕ are now determinable. The temporal variations of ϱV_θ , ϱV_ϕ , and \mathcal{E} are then obtained through equations (B25) and (B27), respectively.

B3. BOUNDARY CONSTRAINTS FOR $NV_r \leq 0$, BC2

In this case, V_r is reset to zero. The other constraint we choose is the fixed adiabatic enthalpy expressed as

$$\frac{\partial}{\partial t} \left(\frac{P_g}{\varrho^\gamma} \right) = 0. \quad (\text{B29})$$

Note that this satisfies the advection equation of the adiabatic flow along the radial direction

$$\left(\frac{\partial}{\partial t} + V_r \frac{\partial}{\partial r} \right) \left(\frac{P_g}{\varrho^\gamma} \right) = 0, \quad (\text{B30})$$

with $V_r = 0$. Because B_θ and B_ϕ are not always zero, equations (B22) and (B23) require V_θ and V_ϕ to be zero. Therefore, we obtain

$$\mathbf{V} = 0, \quad \frac{\partial \mathbf{V}}{\partial t} = 0. \quad (\text{B31})$$

With equations (B20), (B29), and (B31), we obtain the temporal variation of the density expressed in terms of those of other variables,

$$\frac{\partial \varrho}{\partial t} = \frac{\gamma - 1}{\gamma} \frac{\varrho}{P_g} \left(\frac{\partial \mathcal{E}}{\partial t} - B_\theta \frac{\partial B_\theta}{\partial t} - B_\phi \frac{\partial B_\phi}{\partial t} \right). \quad (\text{B32})$$

Finally, we obtain the characteristic equations with three undetermined temporal variations,

$$\left(L_{l5} - \frac{\gamma - 1}{\gamma} \frac{\varrho}{P_g} B_\theta L_{l1} \right) \frac{\partial B_\theta}{\partial t} + \left(L_{l6} - \frac{\gamma - 1}{\gamma} \frac{\varrho}{P_g} B_\phi L_{l1} \right) \frac{\partial B_\phi}{\partial t} + \left(L_{l7} + \frac{\gamma - 1}{\gamma} \frac{\varrho}{P_g} L_{l1} \right) \frac{\partial \mathcal{E}}{\partial t} = \text{RHS}_l. \quad (\text{B33})$$

Because this equation set does not contain B_r in the denominator, this constraint, BC2, is always used when $|B_r|/B$ is smaller than 0.01.

B4. BOUNDARY CONSTRAINTS FOR $NV_r > (NV_r)_c$, BC3a, BC3b, AND BC3ab

In this case, the number flux flowing through the solar surface is reset to be the critical value $(\varrho V_r)_c$. The limitation is expressed as

$$\varrho V_r = (\varrho V_r)_c, \quad \frac{\partial (\varrho V_r)}{\partial t} = 0. \quad (\text{B34})$$

This constraint removes the second terms of equation (B25),

$$\varrho V_r \frac{\partial B_\theta}{\partial t} - B_r \frac{\partial (\varrho V_\theta)}{\partial t} = 0, \quad \varrho V_r \frac{\partial B_\phi}{\partial t} - B_r \frac{\partial (\varrho V_\phi)}{\partial t} = 0. \quad (\text{B35})$$

As the last constraint to be determined, we choose two simple boundary constraints. The first one is to fix the surface temperature (BC3a),

$$\frac{\partial}{\partial t} \left(\frac{P_g}{\varrho} \right) = 0, \quad (\text{B36})$$

and the other one is to fix the density (BC3b),

$$\frac{\partial \varrho}{\partial t} = 0. \quad (\text{B37})$$

Note that these two conditions can be regarded as the extreme cases of the polytrope,

$$\frac{\partial}{\partial t} \left(\frac{P_g}{\varrho^{\gamma'}} \right) = 0, \quad (\text{B38})$$

with the surface specific heat ration $\gamma' \rightarrow 1$ for BC3a and $\gamma' \rightarrow +\infty$ for BC3b. Therefore, we can also define the intermediate choices with $\gamma' = 5/3$ (BC3ab) and $\gamma' = 1.05$ (BC3ab').

To build the characteristic equations to be solved for BC3a and BC3ab, we first obtain

$$\frac{\partial P_g}{\partial t} = \frac{\gamma' P_g}{\rho} \frac{\partial \rho}{\partial t} \quad (\text{B39})$$

from equation (B38). Then, combining with equations (B20), (B34), and (B35), the temporal variation of the total energy can be expressed as

$$\begin{aligned} \frac{\partial \mathcal{E}}{\partial t} &= \mathbf{V} \cdot \frac{\partial(\rho \mathbf{V})}{\partial t} - \frac{V^2}{2} \frac{\partial \rho}{\partial t} + \frac{1}{\gamma - 1} \frac{\partial P_g}{\partial t} + \mathbf{B} \cdot \frac{\partial \mathbf{B}}{\partial t} \\ &= \frac{\rho V_r V_\theta}{B_r} \frac{\partial B_\theta}{\partial t} + \frac{\rho V_r V_\phi}{B_r} \frac{\partial B_\phi}{\partial t} - \frac{V^2}{2} \frac{\partial \rho}{\partial t} + \frac{\gamma' P_g}{(\gamma - 1)\rho} \frac{\partial \rho}{\partial t} + B_\theta \frac{\partial B_\theta}{\partial t} + B_\phi \frac{\partial B_\phi}{\partial t} \\ &= \left[\frac{\gamma' P_g}{(\gamma - 1)\rho} - \frac{V^2}{2} \right] \frac{\partial \rho}{\partial t} + \left(\frac{\rho V_r V_\theta}{B_r} + B_\theta \right) \frac{\partial B_\theta}{\partial t} + \left(\frac{\rho V_r V_\phi}{B_r} + B_\phi \right) \frac{\partial B_\phi}{\partial t}. \end{aligned} \quad (\text{B40})$$

With equations (B34), (B35), and (B40), the characteristic equation (B18) finally becomes determinable:

$$\begin{aligned} \left\{ L_{11} + \left[\frac{\gamma' P_g}{(\gamma - 1)\rho} - \frac{V^2}{2} \right] L_{17} \right\} \frac{\partial \rho}{\partial t} + \left[\frac{\rho V_r}{B_r} L_{13} + L_{15} + \left(\frac{\rho V_r V_\theta}{B_r} + B_\theta \right) L_{17} \right] \frac{\partial B_\theta}{\partial t} \\ + \left[\frac{\rho V_r}{B_r} L_{14} + L_{16} + \left(\frac{\rho V_r V_\phi}{B_r} + B_\phi \right) L_{17} \right] \frac{\partial B_\phi}{\partial t} = \text{RHS}_I, \end{aligned} \quad (\text{B41})$$

with $\gamma' = 1$ for BC3a, $\gamma' = 5/3$ for BC3ab, and $\gamma' = 1.05$ for BC3ab'. The characteristic equations for BC3b,

$$\left(\frac{\rho V_r}{B_r} L_{13} + L_{15} \right) \frac{\partial B_\theta}{\partial t} + \left(\frac{\rho V_r}{B_r} L_{14} + L_{16} \right) \frac{\partial B_\phi}{\partial t} + L_{17} \frac{\partial \mathcal{E}}{\partial t} = \text{RHS}_I, \quad (\text{B42})$$

are obtained from equations (B34), (B35), and (B37).

REFERENCES

- Aschwanden, M. J., & Acton, L. W. 2001, *ApJ*, 550, 475
 Brackbill, J. U., & Barnes, D. C. 1980, *J. Comput. Phys.*, 35, 426
 Briio, M., & Wu, C. C. 1988, *J. Comput. Phys.*, 75, 400
 Cargo, P., & Gallice, G. 1997, *J. Comput. Phys.*, 136, 446
 Detman, T. R., Dryer, M., Yeh, T., Han, S. M., Wu, S. T., & McComas, D. J. 1991, *J. Geophys. Res.*, 96, 9531
 Dryer, M., Smith, Z. K., Coates, A. J., & Johnstone, A. D. 1991, *Sol. Phys.*, 132, 353
 Evans, C. R., & Hawley, J. F. 1988, *ApJ*, 332, 659
 Fisher, R. R., & Guhathakurta, M. 1994, *Space Sci. Rev.*, 70, 267
 Frazin, R. A., & Janzen, P. 2002, *ApJ*, 570, 408
 Gallagher, P. T., Mathioudakis, M., Keenan, F. P., Phillips, K. J. H., & Tsinganos, K. 1999, *ApJ*, 524, L133
 Geiss, J. G., Gloeckler, G., & von Steiger, R. 1995, *Space Sci. Rev.*, 72, 49
 Groth, C. P. T., De Zeeuw, D. L., Gombosi, T. I., & Powell, K. G. 2000, *J. Geophys. Res.*, 105, 25053
 Han, S. M., Wu, S. T., & Dryer, M. 1988, *Comput. Fluids*, 16, 81
 Harten, A. 1983, *J. Comput. Phys.*, 49, 151
 Hoeksema, J. T., & Scherrer, P. H. 1986, *Sol. Phys.*, 105, 205
 Jeffrey, A., & Taniuti, T. 1964, *Non-Linear Wave Propagation* (New York: Academic Press), chaps. 1 and 3
 Linker, J. A., Van Hoven, G., & Schnack, D. D. 1990, *Geophys. Res. Lett.*, 17, 2281
 Linker, J. A., et al. 1999, *J. Geophys. Res.*, 104, 9809
 Mikić, Z., Linker, J. A., Dalton, D., Schnack, D., Lionello, R., & Tarditi, A. 1999, *Phys. Plasmas*, 6, 2217
 Nakagawa, Y. 1980, *ApJ*, 240, 275
 ———. 1981a, *ApJ*, 247, 707
 Nakagawa, Y. 1981b, *ApJ*, 247, 719
 Nakagawa, Y., Hu, Y. Q., & Wu, S. T. 1987, *A&A*, 179, 354
 Nakagawa, Y., & Steinolfson, R. S. 1976, *ApJ*, 207, 296
 Neugebauer, M. 1999, *Rev. Geophys.*, 37, 107
 Parker, E. N. 1958, *ApJ*, 128, 664
 Powell, K. G. 1994, ICASE Report 94-24 (Hampton: NASA Langley Research Center)
 Riley, P., Gosling, J. T., & Pizzo, V. J. 1997, *J. Geophys. Res.*, 102, 14677
 Roe, P. L. 1981, *J. Comput. Phys.*, 43, 357
 Roe, P. L., & Balsara, D. S. 1996, *SIAM J. Appl. Math.*, 56, 57
 Schatten, K. H., Wilcox, J. M., & Ness, N. F. 1969, *Sol. Phys.*, 6, 442
 Schmidt-Voigt, M. 1989, *A&A*, 210, 433
 Smith, Z., & Dryer, M. 1990, *Sol. Phys.*, 129, 387
 Steinolfson, R. S., Suess, S. T., & Wu, S. T. 1982, *ApJ*, 255, 730
 Svalgaard, L., Duvall, T. L., Jr., & Scherrer, P. H. 1978, *Sol. Phys.*, 58, 225
 Tanaka, T. 1995, *J. Geophys. Res.*, 100, 12057
 Tóth, G. 2000, *J. Comput. Phys.*, 161, 605
 Usmanov, A. V. 1993, *Sol. Phys.*, 148, 371
 Usmanov, A. V., & Dryer, M. 1995, *Sol. Phys.*, 159, 347
 Usmanov, A. V., & Goldstein, M. L. 2003, *J. Geophys. Res.*, 108, 1354
 van Leer, B. 1979, *J. Comput. Phys.*, 32, 101
 Wang, A.-H., Wu, S. T., Suess, S. T., & Poletto, G. 1993, *Sol. Phys.*, 147, 55
 Washimi, H., & Sakurai, T. 1993, *Sol. Phys.*, 143, 173
 Wu, S. T., Dryer, M., & Han, S. M. 1983, *Sol. Phys.*, 84, 395
 Wu, S. T., Wang, A. H., & Guo, W. P. 1996, *Ap&SS*, 243, 149
 Wu, S. T., & Wang, J. F. 1987, *Comput. Meth. Appl. Mech. Eng.*, 64, 267
 Wu, S. T., et al. 2001, *J. Geophys. Res.*, 106, 25089
 Yeh, T., & Dryer, M. 1985, *Ap&SS*, 117, 165